Applied Materials Today 29 (2022) 101566

Contents lists available at ScienceDirect

Applied Materials Today

journal homepage: www.elsevier.com/locate/apmt

Laminated antimonene as an alternative and efficient shielding strategy against X-ray radiation

Md J. Nine [a,*], Le Yu [a], Ana L.C. Pereira [a,b], Munkhbayar Batmunkh [c], Kamrul Hassan [a], Alexandre M.C. Santos [d,e], Tran T. Tung [a], Dusan Losic [a,*]

[a] School of Chemical Engineering and Advanced Materials, The University of Adelaide, Adelaide, South Australia 5005, Australia
[b] School of Applied Sciences, University of Campinas (UNICAMP), Limeira 13484-350, Brazil
[c] Queensland Micro- and Nanotechnology Centre, School of Environment and Science, Griffith University, Nathan, Queensland 4111, Australia
[d] School of Physical Sciences, University of Adelaide, Adelaide, South Australia 5005, Australia
[e] Department of Medical Physics, Royal Adelaide Hospital, Adelaide, South Australia 5000, Australia

ARTICLE INFO

Keywords:
Lamination
Antimonene
X-ray shield
Radiation protection

ABSTRACT

Scientific research concerning lead (Pb)-free shielding materials and their composites showed great promise in shielding ionising radiation (e.g., X-ray, gamma-ray) applied in medical diagnosis, security screening, space and nuclear industry. However, the typical "blend and mix" composites with imperfect composition due to random particle distribution, morphology, low density, and unwanted micro-crack in an inappropriate matrix could result in poor X-ray attenuation. To address these limitations, we demonstrate a unique laminated architecture using few-layered antimonene (Sb_{FL}) to increase the chances of interaction between ionising radiation and shielding materials. The proposed lamination is a sandwiched structure (PDMS-Sb_{FL}-PDMS) having an identical composition to a conventional form of composite (PDMS/Sb_{FL}). The experiments were carried out within X-ray energy ranging between ~14 and 35 keV (equivalent tube voltage of 30 to 100 kVp), which was further numerically investigated with an extended energy range up to 100 keV. The PDMS-laminated Sb_{FL} with a cotton carrier exhibited an attenuation enhancement of 45% and ~3 times reduced half-value layers (HVL) at high energy (e.g., ~35 keV) X-ray compared to the conventional PDMS/Sb_{FL} composite (13.5 wt% of Sb_{FL}). Using high-density Sb_{FL} nanoflakes in a sandwiched structure demonstrated significant potential to overcome practical challenges (e.g., aggregation, particle distribution, interparticle gaps, cracks) of composites typically employed for shielding ionising radiation.

1. Introduction

Human exposure to different ionising radiations has become very frequent due to their extensive use in medical imaging [1], radiation therapy [2], airport security checking [3], nuclear fuel imaging [4], diagnosis of structural faults [5], as well as in space industries [6]. In brief, the worldwide yearly exercises of ionising radiation related to the medical industry include more than 3600 million diagnostic radiology examinations, 37 million nuclear medicine procedures, and 7.5 million radiation therapy [7]. Uncontrolled exposure to scattered ionising radiation is well documented to have many adverse health impacts, such as an increase in the risk of deadly acute radiation syndrome (e.g., fatigue, loss of appetite) [8,9], risk of long-term effects on the body (e.g., cancer) [10]. Consequently, wearable shielding has become a common practice to protect against X-ray ionising radiation during the procedures, wherein radiographers and patients widely use lead (Pb) aprons [11–13]. However, the findings revealed that a lead apron of 0.5 mm thickness could block just over one-third of the scattered radiation recommended to minimise frequent human exposure to radiation rather than reliance on protection by Pb aprons [11]. Nowadays, Pb is considered to be less desirable material for use in wearable radiation protection due to its heavy weight (~ 4.95 kg apron weight for 0.50 mm Pb), inflexibility, poor durability, and toxicity [14–16]. Therefore, researchers in the field are putting much efforts to develop an efficient and Pb-alternative radiation protection coatings/films.

In this trend, many medium and high-atomic number (Z) elements (tin (Sn) [17], antimony (Sb) [13], iodine (I) [17], barium (Ba) [17], tungsten (W) [18], bismuth (Bi) [19], thorium (Th) [20], uranium (U)

* Corresponding authors.
E-mail addresses: mdjulker.nine@adelaide.edu.au (M.J. Nine), dusan.losic@adelaide.edu.au (D. Losic).

https://doi.org/10.1016/j.apmt.2022.101566
Received 2 April 2022; Received in revised form 25 May 2022; Accepted 16 June 2022
Available online 23 June 2022

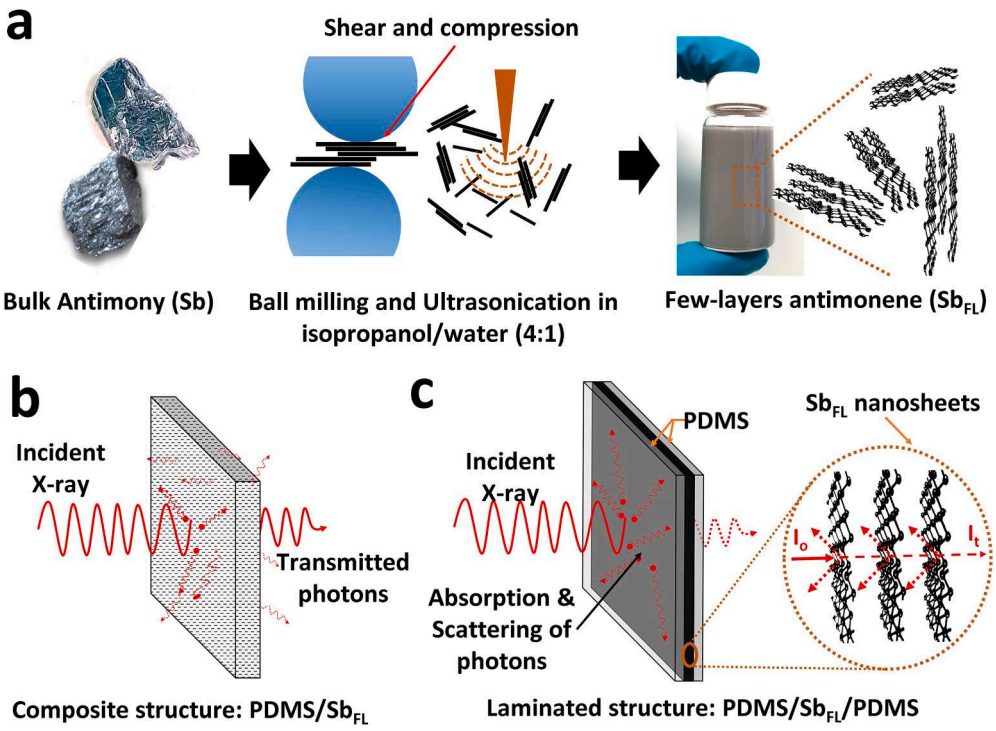

Fig. 1. Schematic representation of the synthesis and film preparation, (a) Mechanical exfoliation of bulk antimony (Sb) combining wet ball-milling and ultrasonication in isopropanol/water (4:1) medium, (b) Conventional PDMS/Sb_{FL} composite structure of X-ray shielding, (c) Laminated approach of X-ray shielding by Sb_{FL} (Sb_{FL} nanoflakes sandwiched between PDMS thin film).

[20], plutonium (Pu) [20], (W-Si) [21] and their oxide compounds such as bismuth(III) oxide (Bi_2O_3) [14,22], copper (II) oxide (CuO) [23], lead (II) oxide (PbO) [22], tungsten oxide (WO_3) [24], cadmium oxide (CdO) [25], gadolinium (III) oxide (Gd_2O_3) [26,27], clay (e.g., dolomite) [28] as well as their blend have been extensively investigated. Recently reported 2D transition metal carbides could be a potential group of materials for enhanced electromagnetic interference (EMI) shielding [29–31]. In addition, a few carbon nanomaterials (e.g., carbon nanotubes (CNTs), graphene) were reported to be effective in EMI shielding [32,33]. The combination of medium and high-Z elements/compounds is an efficient strategy to achieve protection over a broad energy range because of the absorption limit of individual materials against specific energy [13,17,34]. Despite the efforts made for the development of Pb-free protection, the conventional strategy in the fabrication of wearable protective films remained unchanged over many years, which is simply a "blend it and test it" process combining different radiation absorptive materials into polymeric [19,25–27,35,36], or glass matrix [22]. These composites combined with fabrics [14,16], film or paper [18], have been tested to justify their potential for shielding aprons [13,14,16,37]. A few works reported particle size effect in radiation shielding, wherein nanoparticles perform better than microparticles in polymer composites against low radiation energy range [19,23,24]. In this case, the factual reasons for poor attenuation performance lie in unsuitable particle morphology, distribution, crack formation, and the large interparticle gaps within the conventional form of composites. Although X-ray attenuation depends on the density of materials, it is realized that photon-matter interaction reduces due to numerous interparticle gaps, cracks, and inefficient particle morphology appearing in composites.

To address these problems, we framed an elemental 2D material (e.g., antimonene, a few layers of Sb) [38,39], into film with a compact layered structure laminated with PDMS films. The dense laminated structure is proposed to increase the chance of matter-photons interactions. The proposed fabrication method and working principle are illustrated in Fig. 1a–c. A series of layered films composed of Sb_{FL} were prepared on a cotton carrier and encased in a PDMS mould making the laminated composite to demonstrate the hypothesis shown in Fig. 1**c**. The X-Ray shielding performances of the proposed laminated sample were conducted to investigate their X-ray attenuation in an experimental energy range between ~14 and 35 keV (equivalent beam energy of 30 to 100 kVp) and compared with the conventional composite structure (schematically illustrated in Fig. 1**b**). The lower X-ray energy range chosen in this work is based on the X-ray energy frequently used in medical imaging and diagnosis. The simulation results of both composite and laminated samples were performed across a broader energy range (~10 keV up to 120 keV) and compared with experimental results. Relevant photon atomic parameters such as linear attenuation coefficient, half-value layers (HVL), tenth-value layers (TVL), and mass attenuation coefficient were derived and compared. The laminated and layered approach to the structural arrangement of effective shielding materials with larger K-edge values could be future follow-up work to attenuate ionized radiation with higher energy.

2. Materials and methods

2.1. Materials

Bulk crystalline antimony (Sb) with 99.9% purity was purchased from Smart Elements, Austria. The elastomeric polydimethylsiloxane (PDMS) prepolymer (Sylgard 184) with a curing agent was obtained from Dow Corning Corporation (USA). Other chemicals such as Isopropanol (reagent grade, ≥ 99.5%), toluene (anhydrous, 99.8%) were purchased from Merck, Australia. Milli-Q water (PURELAB Option-Q, 18.2 MΩ cm) was used in the experiments. Thin white cotton fabric was purchased from a local supplier, "Lincraft", South Australia.

2.2. Exfoliation of bulk Sb

Few-layer antimonene (Sb_{FL}) nanosheets were prepared in a 4:1 isopropanol/water mixture by exfoliating bulk Sb crystals using a

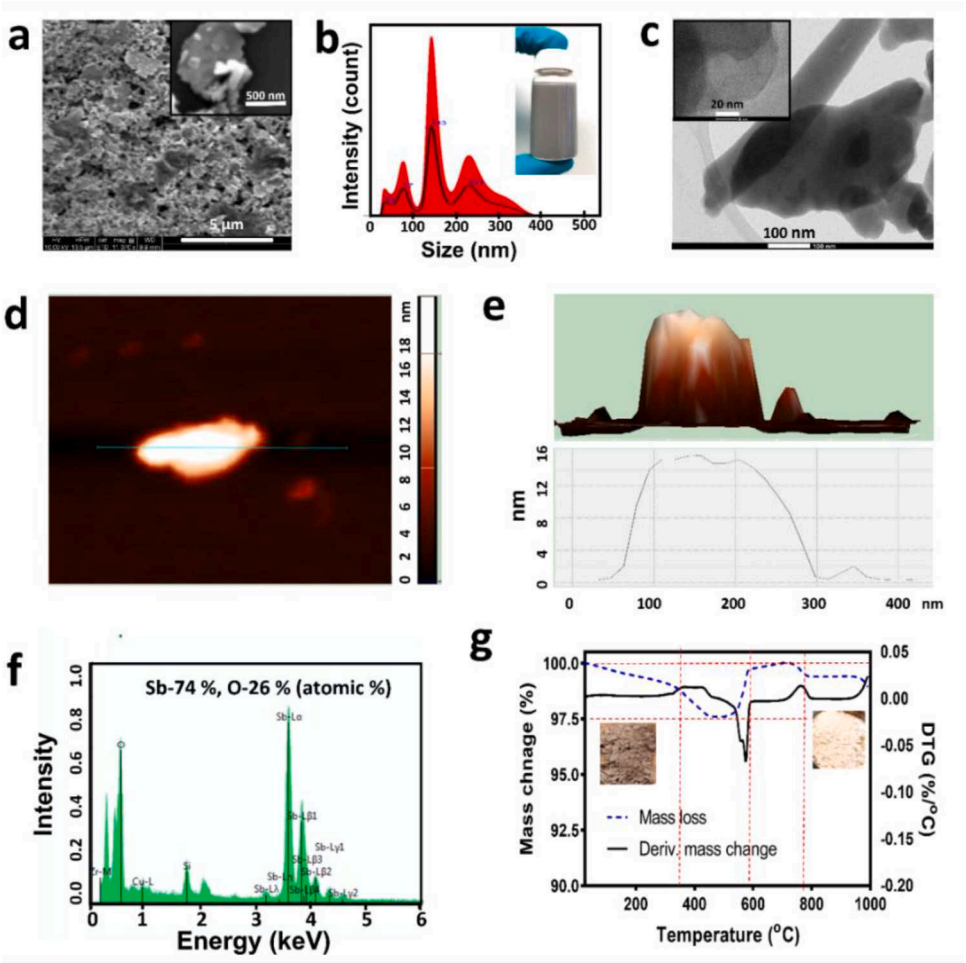

Fig. 2. Structural and chemical properties of exfoliated Sb_{FL}. (a) SEM micrograph of Sb_{FL}, (b) Particle size distribution (Inset image-dispersed Sb_{FL} in Isopropanol), (c) high-resolution TEM image of Sb_{FL}, (d) AFM of Sb_{FL}, (e) line profile showing thickness of the Sb_{FL}, (f) EDX spectrum of Sb_{FL}, (g) TGA and DTG of Sb_{FL}.

combination of ball milling and ultrasonication. Bulk Sb crystals (1 g/pot) were put in a zirconia milling pot (150 ml) with isopropanol/water solvent (50 ml/pot). The samples were then ball-milled using a Retsch planetary ball mill (PM 200) with zirconia balls (3 mm size, 50 ml/pot) at 300 rpm for 3 h. After drying, the ball-milled Sb flakes (10 mg/ml) were re-dispersed in 4:1 isopropanol/water mixture for further exfoliation using a tip-ultrasonication sonicator (Digital Sonifier 450, Branson) for 40 min. Then the resulting black suspension was centrifuged at 3000 rpm for 3 min, and the dark grey supernatant was recovered and oven-dried at 50 °C.

2.3. Preparation of testing films

The exfoliated Sb_{FL} powder was further dispersed into toluene by ultrasonication using a tip-sonicator (Digital Sonifier 450, Branson). The Sb_{FL} suspension was added to PDMS prepolymer at three different loading% (4.5 wt%, 9.0 wt%, 13.5 wt%) and mixed in a beaker using an overhead mechanical stirrer (IKA RW20 digital). Once the toluene evaporated, the curing agent was mixed in the beaker to prepare the final PDMS/Sb_{FL} semi-solid composite, which was poured into a Teflon mould (2.5 cm × 2.5 cm) to prepare PDMS/Sb_{FL} films. The thickness of the prepared films (as tabulated in **Table S2**) was maintained by pouring an identical volume of casting materials (e.g., PDMS and PDMS-based composite).

In case of laminated sample, PDMS film with a square size dip (2.5 cm × 2.5 cm × 0.5 mm) in the middle was prepared which was used as negative template. An ethanol soaked wet-cotton fabric (2.5 cm × 2.5 cm) was placed on a negative PDMS template as Sb_{FL} nanosheets carrier. Then, the desired amount of ethanol-based Sb_{FL} suspension was drop cast on the fabrics and allowed to dry at room temperature to fabricate Sb_{FL} films, as shown in Fig. S3. Finally, a measured amount of PDMS prepolymer mixed with a curing agent (part-A and part-B) was poured on the cast film to cover the dip area and thermally cured at 50 °C in the oven for 48 h. (Characterization and X-ray radiation measurement experiment details are provided in **Supporting Information**)

3. Results and discussion

The morphology, elemental analysis, and thermal properties of exfoliated Sb_{FL} sheets are presented in Fig. 2. The morphology of exfoliated bulk-Sb was demonstrated in Fig. 2**a**, wherein the few-layered nano/micro-flakes (confirmed by the inset image) are randomly distributed all over the surface. The flake size distribution of the exfoliated Sb_{FL} was in a broad range between 100 and 300 nm, in which dominated peak counts of particle distribution were determined between 100 and 200 nm, as displayed in Fig. 2**b**. The high-resolution transmission electron microscope (TEM) image in Fig. 2**c** presents exfoliated Sb_{FL} flakes overlapping adjacent layers. The average thickness of random particles was realized by the atomic force microscope (AFM) image demonstrated in Figs. 2**d, e** and **S2**, showing multi-layer exfoliation with approximately 16 nm thick, corresponding to ~35–40 atomic layers Sb_{FL} [40]. The characteristic elemental peaks of Sb_{FL} indicate the presence of oxygen in the materials suggesting the partial oxidation of

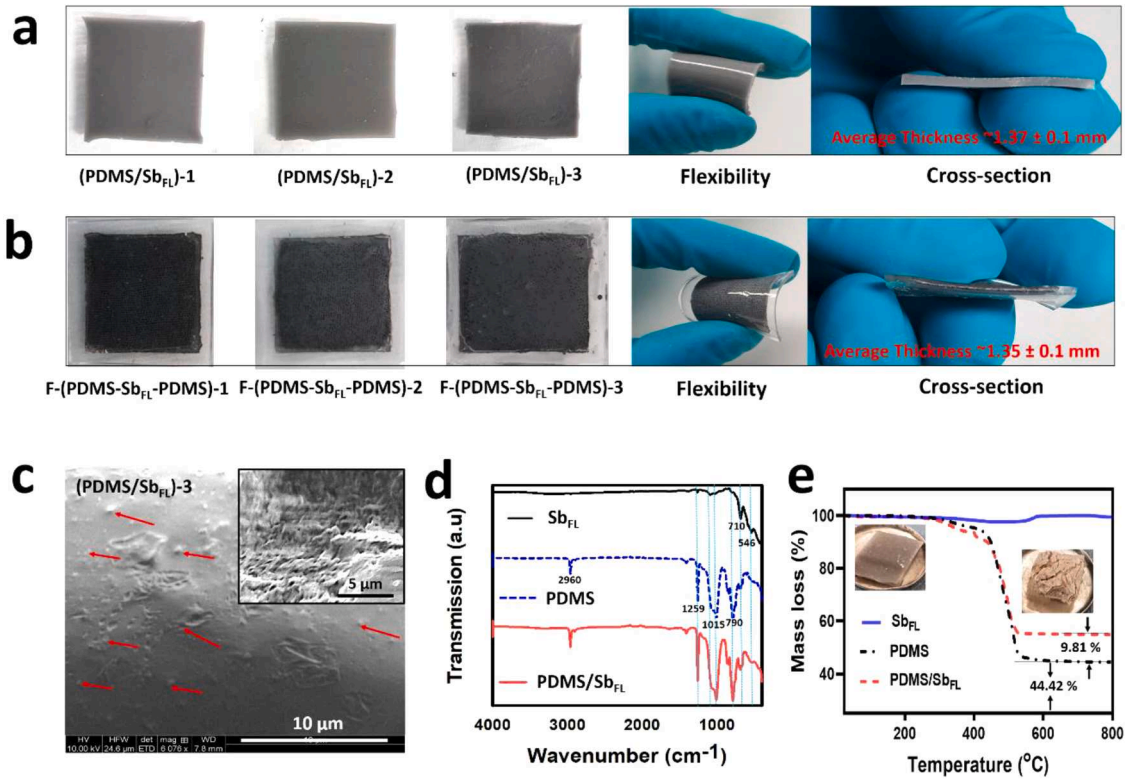

Fig. 3. Prepared films in conventional composite approach and sandwiched structure, (a) Composite films (PDMS/Sb$_{FL}$)-1, (PDMS/Sb$_{FL}$)-2 and (PDMS/Sb$_{FL}$)-3 corresponding to 4.5 wt%, 9 wt% and 13.5 wt%, respectively. The flexibility (inset-middle) of composite films with an average thickness of 1.37± 0.1 mm. (b) Laminated films with intermediate cotton fabric as Sb$_{FL}$ carrier. F-(PDMS-Sb$_{FL}$-PDMS)-1, F-(PDMS-Sb$_{FL}$-PDMS)−2 and F-(PDMS-Sb$_{FL}$-PDMS)-3 corresponding to 4.5 wt%, 9 wt% and 13.5 wt%, respectively. The flexibility (inset-middle) of composite films with an average thickness of 1.35 ± 0.1 mm. (c) SEM of the composite film (PDMS/Sb$_{FL}$)−3. (d) Characteristic FTIR peaks of Sb$_{FL}$, PDMS and PDMS/Sb$_{FL}$. (e) Comparative mass-change profile of Sb$_{FL}$, PDMS and PDMS/Sb$_{FL}$ (Air atmosphere) during thermogravimetric analysis.

Sb$_{FL}$ flakes either during or after the exfoliation (Fig. 2**f**). Energy-dispersive X-ray spectroscopy (EDX) showed that the quantified atomic composition for oxygen is 26%, while the rest is Sb. Thermal degradation of the Sb$_{FL}$ was demonstrated using thermogravimetric analysis (TGA) and derivative thermogravimetry (DTG), as depicted in Fig. 2**g**. Although the sample was preheated at 50 °C, it retained approximately ~1.5 wt% of moisture, leaving the sample between 100 and 150 °C. There is still a mass loss of ~2 wt.% between 320 and 580 °C, which might be caused by the unwanted impurities in the sample involved during the exfoliation of Sb$_{FL}$. The conversion of grey colour Sb$_{FL}$ into white (shown in the inset image) indicates complete oxidation in an air atmosphere at an elevated temperature between 500 and 800 °C. In the third stage, at a temperature around 580 °C, a significant increase in the mass was observed due to the oxidation of Sb$_{FL}$, resulting in white antimony (III) oxide (Sb_2O_3).

With an intention to improve the ability to attenuate ionizing radiation (e.g., X-ray), laminated film with sandwiched "PDMS-Sb$_{FL}$-PDMS" structure was proposed in this work as an alternative to the conventional "blend-and-mix" type composite, e.g., "PDMS/Sb$_{FL}$" wherein both types of the specimen should contain identical composition for comparison. The "PDMS/ Sb$_{FL}$" composite films with three different weight percentages (4.5 wt%, 9 wt% and 13.5 wt%) of Sb$_{FL}$ were labelled as (PDMS/Sb$_{FL}$)-1, (PDMS/Sb$_{FL}$)-2 and (PDMS/Sb$_{FL}$)-3, respectively, as shown in Fig. 3**a**. The film fabrication with sandwiched "PDMS-Sb$_{FL}$-PDMS" structure was challenging as micro-cracks formed in the middle layer caused by thermal shrinkage of Sb$_{FL}$ on PDMS mould, as shown in **Fig. S3a–c**. Toward the tentative formation of the crack-free film, graphene oxide (GO), and rosin were employed as a binder, wherein GO was identified to be a crack enhancer, and rosin influenced the aggregation of Sb$_{FL}$ (**Fig. S3a–c**). Finally, the use of cotton fabric as Sb$_{FL}$ carrier in the laminated samples (F-(PDMS-Sb$_{FL}$-PDMS)-1, F-(PDMS-Sb$_{FL}$-PDMS)-2 and F-(PDMS-Sb$_{FL}$-PDMS)−3) provided crack-free samples as shown in Figs. 3**b** and **S4b**. For the comparison, these samples of conventional composites and laminated sandwiched structures were prepared with identical wt% of Sb$_{FL}$ and PDMS for each composition, as shown in **Table S2**. The deposition of mid-layer "Sb$_{FL}$" for the mass of 30 mg, 60 mg and 90 mg (corresponding to 4.5 wt%, 9 wt% and 13.5 wt % of Sb$_{FL}$) resulted in 51 ± 3 µm, 111 ± 3 µm and 165 ± 3 µm of thickness, respectively (**Fig. S5a–c**). The laminated samples are "Sb$_{FL}$" loaded cotton fabrics sandwiched by PDMS films, as shown in Fig. 3**b**. Both composite and laminated films were flexible (inset-middle) with an average thickness of 1.37 ± 0.1 mm and 1.35 ± 0.1 mm, respectively. Fig. 3**c** displays the surface morphology of composite film (e.g., (PDMS/Sb$_{FL}$)-3), while the inset image with a scratch on it revealed the presence of Sb$_{FL}$ (red-arrow and rough) in the PDMS matrix. The chemical and thermal characteristics of the composite films were demonstrated in Fig. 3**d** and **e**. Considering the partial oxidation of Sb$_{FL}$ during ball-milling (Fig. 2**f**), FTIR characteristic peaks were expected to correspond to Sb—O—Sb and Sb—O vibration bond. According to the literature, four distinct FTIR peaks of Sb_2O_3 could be generated. Herein, a couple of low-intensity peaks at 710 and 546 cm^{-1} could be related to asymmetric bending of Sb—O—Sb and asymmetric stretching of Sb—O bond, respectively, as shown in Fig. 3**d** [41,42]. PDMS characteristic FTIR peaks at 1259 cm^{-1} correspond to the deformation or in-plane bending of Si—CH_3, and 789–796 cm^{-1} relates to the out-of-plane oscillations of the Si—CH_3 (rocking vibration mode of −CH_3 and stretching vibration of Si—C in Si-CH_3). The FTIR peaks at 1000–1074 cm^{-1} and 2950–2960 cm^{-1} are due to stretching of Si—O—Si and asymmetric stretching in Si—CH_3, respectively [43,44]. Recorded data from thermogravimetric analysis (TGA) of Sb$_{FL}$, PDMS and PDMS/Sb$_{FL}$ samples

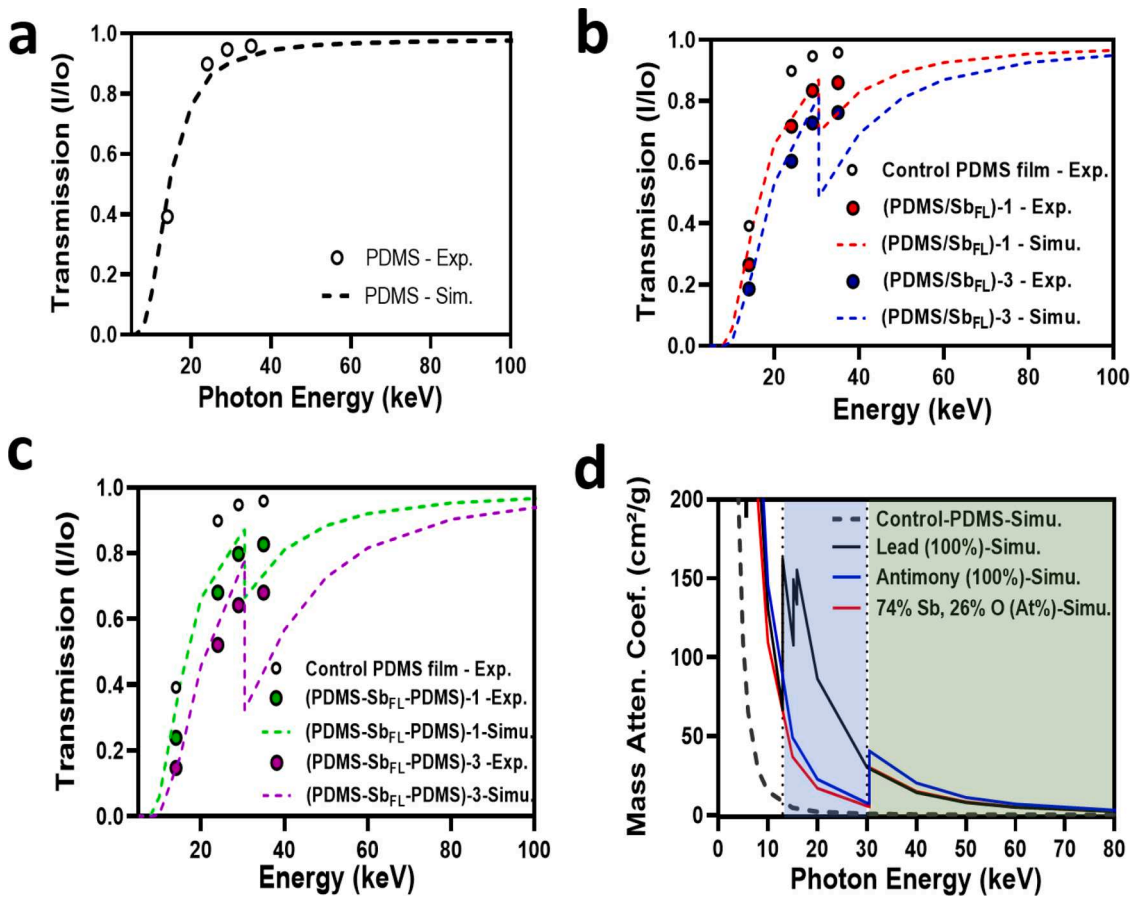

Fig. 4. Comparison of experimental and numerical simulation results of X-ray transmission through Control-PDMS, PDMS/Sb_{FL} composites and laminated samples. (a) PDMS films (1.38 mm thickness), (b) X-ray transmission through composite films ((PDMS/Sb_{FL})-1, and (PDMS/Sb_{FL})-3) (c) X-ray transmission through laminated films ((PDMS-Sb_{FL}-PDMS)-1, and (PDMS-Sb_{FL}-PDMS)-3), (d) Direct comparison of numerically simulated mass attenuation coefficients (pure PDMS, 100% Pb, 100% Sb, and "74% Sb-26% O (atomic%)" with the composite films (experimental) of (PDMS/Sb_{FL})-3 and (PDMS-Sb_{FL}-PDMS)-3.

were plotted in Fig. 3**e**. Different mass change profiles of Sb_{FL}, PDMS and PDMS/Sb_{FL} specimens were observed while undergoing a thermal degradation in the air atmosphere. Thermal degradation of Sb_{FL} was discussed above in detail, as displayed in Fig. 2**g**, while a two-stage mass loss was distinguished for PDMS. The 1st stage mass loss took place at an on-set temperature of ~281 °C with a maximum decomposition temperature (T_{max-1}) at 330 °C. With a maximum decomposition, the second stage mass-loss was identified at around 502 °C [45]. An identical mass loss profile was observed for "PDMS/Sb_{FL}" composite except for the additional ~9.81% residual mass due to the presence of oxidised Sb_{FL} (Sb_2O_3). The inset-images in Fig. 3**e** indicate the physical change before and after thermal decomposition of PDMS/Sb_{FL}.

The transmitted intensity of X-rays (I/I_0) for the samples (control PDMS film, PDMS/ Sb_{FL} composites and laminated "PDMS-Sb_{FL}-PDMS" samples) were examined and analysed both experimentally and numerically, as presented in Fig. 4. Details about the experimental measurements and the simulations are provided in **Section 3.4** of **Supporting Information**. Considering the density of PDMS ($\rho = 0.97$ g/cm^3) film with a measured thickness of 1.38 ± 0.1 mm, X-ray transmission values expected from the simulations are in excellent agreement with the experimental outcome, as shown in Fig. 4**a**. It is obvious that despite posing ~ 60% attenuation effect at low energy X-ray (14 keV), control PDMS film has an insignificant X-ray attenuation effect at 35 keV, showing ~96% of X-ray transmission at the defined thickness. Fig. 4**b** displays X-rays transmission through (PDMS/Sb_{FL})-1 (1.38 mm ± 0.1 mm thick composite film, $\rho_{comp-1} = 0.99$ g/cm^3, 95.4 wt% PDMS and 4.6 wt% Sb_{FL}) and (PDMS/Sb_{FL})-3 (1.41 mm ± 0.1 mm thick film, $\rho_{comp-3} = 1.12$ g/cm^3, 86.6 wt% PDMS and 13.4 wt% Sb_{FL}) as a function of the photon energy at 14, 24, 29 and 35 keV.

The measured physical parameters for the films were considered to simulate the transmitted intensity of X-rays photons. The comparison of X-ray transmission values for "PDMS/Sb_{FL}" composites obtained from simulations and the experiments is also in good agreement. The inclusion of 13.4 wt% Sb_{FL} nano/micro flakes in the PDMS matrix posed significant attenuation, which is approximately 20.4% more effective to attenuate high energy (35 keV) X-ray than control PDMS film. Using the measured and calculated density (**Section S1**), a simulation of X-ray transmission was numerically analysed for laminated composites and compared with the experimental outcome, as shown in Fig. 4**c**. Similar compositions of composites were considered for laminated samples ((PDMS-Sb_{FL}-PDMS)-1 and (PDMS-Sb_{FL}-PDMS)-3). The density of the intermediate Sb_{FL} layer was measured to be $\rho(Sb_{FL}) = 2.14$ g/cm^3, which is much less than the bulk density of Sb ($\rho_{Sb} = 6.697$ g/cm^3). It is important to highlight that the experimental measurements close to the absorption energy (K-shell) of antimony (at 30.5 keV) are not expected to follow precisely the abrupt change in transmission values obtained in simulation. This occurs as the experimental measurements were performed by considering the effective energy of the X-ray beam, which contains a spectrum of peak photon energies instead of a monoenergetic X-ray beam. That explains the inconsistency between experiment and simulation values observed close to the absorption energy in Fig. 4**b** and **c. Fig. S5** shows dose-dependent X-ray transmission through the specimen of composites and laminated structure (fabrics as a carrier). However, Figs. 4**b, c** and **S6** displayed a gradual reduction in X-ray transmission with the increase in loading% of Sb_{FL} for both conventional composite structures and laminated samples.

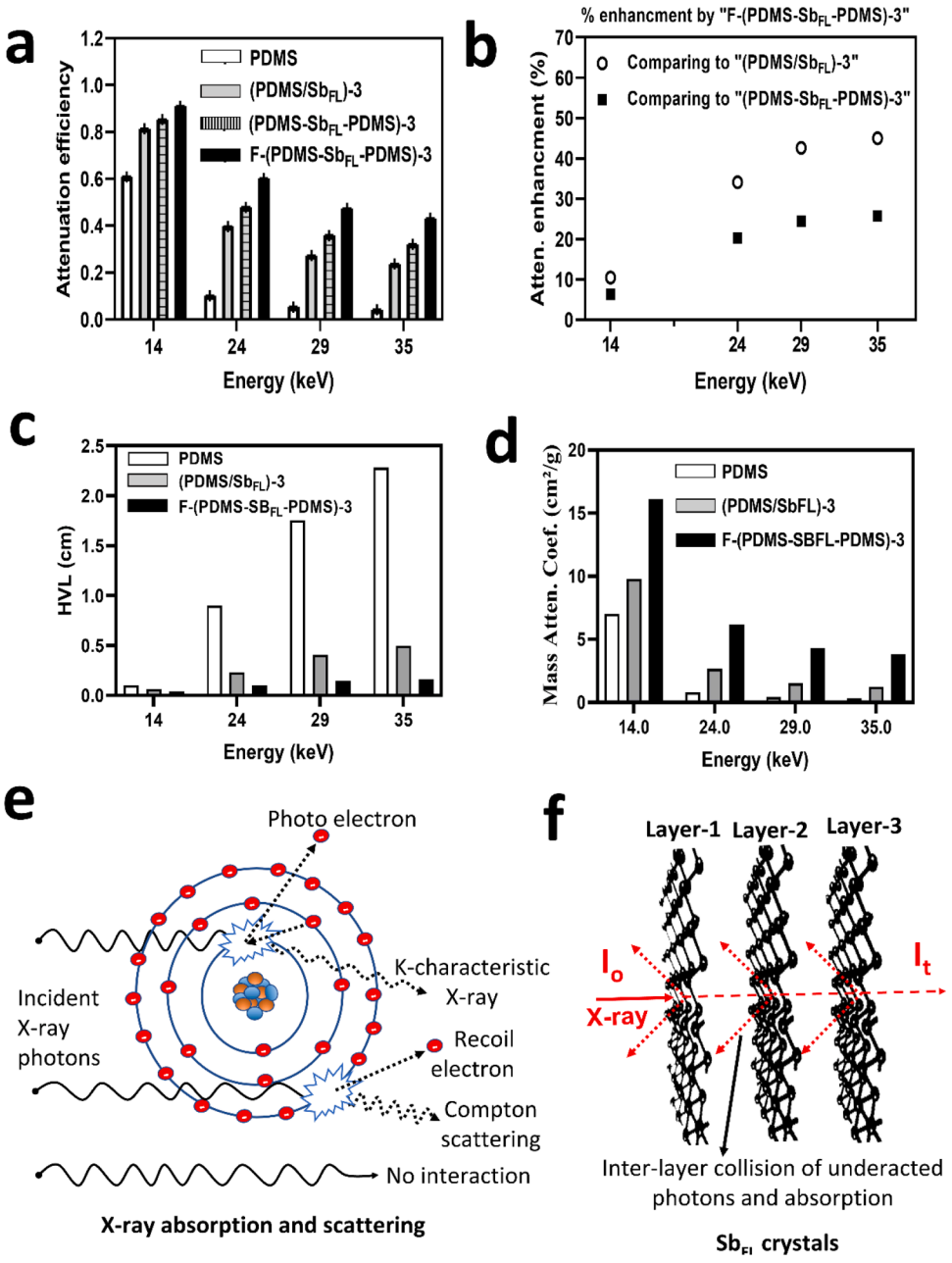

Fig. 5. X-ray attenuation efficiency and enhancement by composite and laminated films (with and without the fabrics carrier) within an energy range between ~14 and 35 keV. (a) Calculated attenuation efficiency obtained by samples of control-PDMS, conventional composite ((PDMS/Sb_{FL})-3), a laminated film without fabrics carrier ((PDMS/Sb_{FL})-3), and laminated film with fabrics carrier (F-(PDMS-Sb_{FL}-PDMS)-3) at different energy band, (b) Enhancement in attenuation by best-performed sample F-(PDMS-Sb_{FL}-PDMS)-3 with respect to (PDMS/Sb_{FL})-3, (PDMS-Sb_{FL}-PDMS)-3 samples. (c) comparison of HVL value for control-PDMS, (PDMS/Sb_{FL})-3, (PDMS-Sb_{FL}-PDMS)-3 samples, (d) comparison of mass attenuation coefficients for control-PDMS, (PDMS/Sb_{FL})-3, (PDMS-Sb_{FL}-PDMS)-3 samples, (e) Generic mechanism of X-ray absorption and scattering, (f) Proposed mechanism of an enhanced interaction between few-layer nanosheets and X-ray.

In Figs. 4**d** and **S7**, the NIST XCOM database was used to calculate the total mass attenuation coefficient for control PDMS, lead (Pb, $Z = 82$), antimony (Sb, $Z = 51$), and the composition of Sb_{FL} containing 74% Sb-26% O (atomic%). Pb was used as a reference to investigate theoretical X-ray attenuation imposed by the materials used in this experiment. The attenuation coefficient curve for Sb_{FL} (74% Sb and 26% O) are very close to the curve posed by 100% Sb, which is different from the Pb curve. In Fig. 4**d**, The discontinuities in the Pb curve (**marked blue shade**) are due to absorption edges (K, L, M) reflecting on the photoelectric absorption. As photoelectric absorption is the dominant process for energies less than 100 keV, the contributions of incoherent scattering and pair production in the nuclear field are less considered. It is noticeable that "Sb" has a slightly better mass attenuation co-efficient than "Pb" after the energy range ~30 keV.

The performance of Pb as a standard X-ray shielding material was compared to relatively low-Z element "Sb" for understanding their effectiveness as a function of the photon energy, as shown in **Fig. S7**. The shielding effectiveness against X-ray radiation of laminated specimen in the presence of a "cotton fabrics carrier" loaded with 13.4 wt% of Sb_{FL} was presented in Fig. 5. Significantly higher transmittance values for both composite and cracked laminated specimens were recorded in contrast to the relatively low X-ray transmission recorded for crack-free laminated nanosheets for the identical loading of Sb_{FL} (Fig. 5**a**). The attenuation enhancement by "F-(PDMS-Sb_{FL}-PDMS)-3″ was as high as 45% compared to the composite "(PDMS/Sb_{FL})-3″ that is 25.75% more than "(PDMS-Sb_{FL}-PDMS)-3″ when high-energy (35 keV) X-ray is applied as shown in Fig. 5**b**. It is highly significant that a rising trend of attenuation enhancement posed by "F-(PDMS-Sb_{FL}-PDMS)-3″ was observed with the increase in X-ray energy. The outcome might be explained by the exponential relationship between the number of photons reaching a specific point and the thickness of the shielding material used. Every photon has a different travel range before it interacts with the shielding atom on its way of transmission. In this regard, HVL and TVL are also frequently used photon atomic parameters to quantify both

Table 1
Benchmark comparison in X-ray transmission at an effective energy of 29 keV (tube voltage 80 kVp).

Specimen	Thickness	% Loading	% Transmission	Refs.
Bi_2O_3/PVC composite (loaded in Nylon fabrics)	1.47 mm	23.08 wt %	46	[14]
Bi_2O_3/PDMS	1.3 mm	28.57 wt %	~48 ± 1	[35]
$BaSO_4$/Silicon rubber (Loaded in cotton fabrics)	~0.4 mm	60 wt%	~78.5	[48]
W/Silicon rubber (Loaded in cotton fabrics)	~0.4 mm	60 wt%	~64	[48]
F-(PDMS-Sb_{FL}-PDMS)-3 (Loaded in cotton fabrics)	1.33 mm	13.5 wt %	52.6	This work

the shielding ability of specific objects and the penetrating ability of specific radiations. The HVL and TVL are the thickness of a radiation shielding material that reduces the radiation level by one-half and one-tenth of the initial level, respectively [46]. In **Fig. 5c**, the HVL value was significantly reduced by laminated samples compared to both control-PDMS and composite against broad range X-ray energy. The effective thickness reduction by the laminated sample "F-(PDMS-Sb_{FL}-PDMS)-3″ is ~14 times and ~3 times less than "control-PDMS" and "(PDMS/Sb_{FL})-3″ samples, respectively, at high-energy (35 keV) X-ray. The calculated HVL and TVL values at different X-ray energy have been tabulated in **Table S3**. Similarly, the enhanced mass attenuation coefficient was obtained by laminated sample "F-(PDMS-Sb_{FL}-PDMS)-3″, which is about ~3 times more than conventional composite blends "(PDMS/Sb_{FL})-3″ at 35 keV as presented in **Fig. 5d**. The outcome with enhanced mass attenuation and reduced HVL value posed by the laminated sample can justify the effectiveness of this new structure proposed in this work. The calculated linear attenuation coefficient shows a few degree improvements in attenuation posed by laminated samples, particularly at higher energy, as plotted in Fig. S8. Although the dominant photoelectric effect is highly active within the energy range between 10 and 30 keV, many incident photons generate scattered radiation after interacting with electrons in the atom through Compton scattering (**Fig. 5e**). It seems that the reduced interparticle gap in the laminated Sb_{FL} structure played a significant role in the reduction of scattered ionizing radiation. The use of multiple succeeding layers (**Fig. 5f**) in the few-layer nanosheets of Sb_{FL} could be a promising strategy to attenuate ionizing radiation. The networking of the fabric structure provides better support for the homogeneous distribution of Sb_{FL} in the laminated PDMS film and contributes to minimising voids and cracks, as shown in **Fig. 3c**. Hence, crack-free compact Sb_{FL} nanosheets in the middle of a sandwiched structure may perform better than dispersed Sb_{FL} in the composite within an identical defined volume.

In this work, the best attenuation performance was obtained by developing a crack-free laminated sample (F-(PDMS-Sb_{FL}-PDMS)-3), wherein a cotton fabric was used as a carrier of Sb_{FL} (18.5 mg/cm^2) sandwiched by PDMS-film. The X-ray transmission results at effective energy of 29 keV (tube voltage 80 kVp) posed by the specimen of F-(PDMS-Sb_{FL}-PDMS)-3 were compared (**Table 1**) with standard 0.18 mm thick Pb sheets equivalent and bismuth oxide/polyvinyl chloride (Bi_2O_3/PVC) composite coated fabrics (Nylon and Polyester) published elsewhere [14,47]. It is noticeable that ~23 wt% of Bi_2O_3/PVC composite coated on Nylon with a thickness of 1.47 mm is reasonably comparable to 13.5 wt% of Sb_{FL} (Sb 74%, O 26% (~Sb_3O)) laminated specimen (F-(PDMS-Sb_{FL}-PDMS)-3) with an approximate thickness of 1.33 mm. However, if the Bi_2O_3/PVC loading is increased to 50% on polyester fabrics with a thickness of just above 1 mm, the coated fabrics transmit 26% of X-ray at 29 keV. The results suggest that four times more loading of a high-Z (Bi = 83) oxide composite (Bi_2O_3/PVC) can generate only two times more effective than the laminated version of relatively low-Z (Sb = 51) compound (Sb_{FL} (Sb_3O)). This comparison reflects a similar outcome achieved in our experiments that the laminated specimen performs ~1.5 times better at an effective X-ray energy of 29 keV than the composite version of the specimen containing an identical loading percentage of Sb_{FL} (13.4 wt%). Similar works based on Bi_2O_3/PDMS (28.57 wt%, 1.3 mm), $BaSO_4$/Silicon rubber (60 wt%, ~0.4 mm), and W/Silicon rubber (60 wt%, ~0.4 mm) composite coated on fabrics performed lower than the outcome of Sb_{FL} (13.4 wt%, 1.33 mm) as enlisted in **Table 1**.

3. Conclusion

A new and efficient shielding strategy was developed by introducing a laminated Sb_{FL} structure to overcome the drawbacks (e.g., aggregation, poor particle distribution, interparticle gaps, cracks) observed in conventional polymer composites. The lamination of Sb_{FL} nanosheets, loaded on a cotton fabrics carrier of F-(PDMS-Sb_{FL}-PDMS)-3 allows ~35% less X-ray transmission over a broad energy range of X-ray (24–35 keV) compared to the composite (PDMS/ Sb_{FL})-3 prepared by conventional "blend and mix" method. The attenuation enhancement by the proposed laminated sample "F-(PDMS-Sb_{FL}-PDMS)-3″ was 45% more than the conventional form of composite "(PDMS/Sb_{FL})-3″ subjected to high energy X-ray (35 keV). Furthermore, the HVL and TVL thickness were significantly reduced by "F-(PDMS-Sb_{FL}-PDMS)-3″ which is ~3 times less than "(PDMS/Sb_{FL})-3″ at 35 keV. The enhanced attenuation was feasibly posed by the Sb_{FL} nanosheets with reduced interparticle gap and their crack-free lamination, which influenced the interaction between photons and shielding atoms. This new design of shielding materials and achieved preference outcome presented in this work is believed to advance the shielding technology of ionizing radiation.

CRediT authorship contribution statement

Md J. Nine: Conceptualization, Visualization, Methodology, Formal analysis, Writing – original draft. **Le Yu:** Methodology, Writing – review & editing. **Ana L.C. Pereira:** Formal analysis, Writing – review & editing. **Munkhbayar Batmunkh:** Writing – review & editing. **Kamrul Hassan:** Writing – review & editing. **Alexandre M.C. Santos:** Methodology, Resources, Writing – review & editing. **Tran T. Tung:** Writing – review & editing. **Dusan Losic:** Supervision, Resources, Formal analysis, Writing – review & editing.

Declaration of Competing Interest

The authors declare that they have no known competing financial interests or personal relationships that could have appeared to influence the work reported in this paper.

Acknowledgments

The authors thank the support of the Australian Research Council (IH 150100003 ARC Research Hub for Graphene Enabled Industry Transformation). This work was also supported in part by the São Paulo Research Foundation (FAPESP) under Grant# 2018/15842-0. Furthermore, we thank The University of Adelaide for providing access to necessary research facilities and support.

Supplementary materials

Supplementary material associated with this article can be found, in the online version, at doi:10.1016/j.apmt.2022.101566.

References

[1] M. Hoheisel, Review of medical imaging with emphasis on X-ray detectors, Nucl. Instrum. Methods Phys. Res. Sect. A Accel. Spectrom. Detect. Assoc. Equip. 563 (1) (2006) 215–224.
[2] M. Goitein, M. Jermann, The relative costs of proton and X-ray radiation therapy, Clin. Oncol. 15 (1) (2003) S37–S50.
[3] D. Turcsany, A. Mouton, T.P. Breckon, Improving feature-based object recognition for X-ray baggage security screening using primed visualwords, in: Proceedings of the IEEE International Conference on Industrial Technology (ICIT), 2013.
[4] H.M.O.D. Parker, M.J. Joyce, The use of ionising radiation to image nuclear fuel: a review, Prog. Nucl. Energy 85 (2015) 297–318.
[5] P.J. Withers, M. Preuss, Fatigue and damage in structural materials studied by X-ray tomography, Annu. Rev. Mater. Res. 42 (1) (2012) 81–103.
[6] M. Durante, F.A. Cucinotta, Physical basis of radiation protection in space travel, Rev. Mod. Phys. 83 (4) (2011) 1245–1281.
[7] World Health Organization (WHO), Ionizing Radiation, Health Effects and Protective Measures, World Health Organization (WHO), 2016, 29 April.
[8] E.H. Donnelly, et al., Acute radiation syndrome: assessment and management, South. Med. J. 103 (6) (2010) 541–546.
[9] F.A.J. Mettler, A.K. Gus'kova, I. Gusev, Health effects in those with acute radiation sickness from the chernobyl accident, Health Phys. 93 (5) (2007) 462–469.
[10] E.S. Gilbert, Ionising radiation and cancer risks: what have we learned from epidemiology? Int. J. Radiat. Biol. 85 (6) (2009) 467–482.
[11] S.J. Hyun, et al., Efficiency of lead aprons in blocking radiation - how protective are they? Heliyon 2 (5) (2016) e00117.
[12] S.H. Hosseini, M. Askari, S.N. Ezzati, X-ray attenuating nanocomposite based on polyaniline using Pb nanoparticles, Synth. Met. 196 (2014) 68–75.
[13] S. Johansen, et al., Are antimony-bismuth aprons as efficient as lead rubber aprons in providing shielding against scattered radiation? J. Med. Imaging Radiat. Sci. 49 (2) (2018) 201–206.
[14] H.A. Maghrabi, et al., Bismuth oxide-coated fabrics for X-ray shielding, Text. Res. J. 86 (6) (2015) 649–658.
[15] M. Zuguchi, et al., Usefulness of non-lead aprons in radiation protection for physicians performing interventional procedures, Radiat. Prot. Dosim. 131 (4) (2008) 531–534.
[16] S.C. Kim, J.R. Choi, B.K. Jeon, Physical analysis of the shielding capacity for a lightweight apron designed for shielding low intensity scattering X-rays, Sci. Rep. 6 (1) (2016) 27721.
[17] E.W. Webster, Experiments with Medium-Z Materials for Shielding Against Low-Energy X Rays, Radiology 86 (1) (1966) 146.
[18] H. Monzen, et al., Estimation of the shielding ability of a tungsten functional paper for diagnostic x-rays and gamma rays, J. Appl. Clin. Med. Phys. 18 (5) (2017) 325–329.
[19] Q. Li, et al., Enhanced radiation shielding with conformal light-weight nanoparticle–polymer composite, ACS Appl. Mater. Interfaces 10 (41) (2018) 35510–35515.
[20] R.B. Roof, X-ray absorption coefficients of thorium, uranium, and plutonium—experimental determination and theoretical interpretation, Phys. Rev. 113 (3) (1959) 820–825.
[21] M. Kazempour, et al., Assessment of the radiation attenuation properties of several lead free composites by monte carlo simulation, J. Biomed. Phys. Eng. 5 (2) (2015) 67–76.
[22] E.S.A. Waly, G.S. Al-Qous, M.A. Bourham, Shielding properties of glasses with different heavy elements additives for radiation shielding in the energy range 15–300 keV, Radiat. Phys. Chem. 150 (2018) 120–124.
[23] M.Z. Botelho, et al., X-ray transmission through nanostructured and microstructured CuO materials, Appl. Radiat. Isot. 69 (2) (2011) 527–530.
[24] N.Z. Noor Azman, et al., Effect of particle size, filler loadings and x-ray tube voltage on the transmitted x-ray transmission in tungsten oxide—epoxy composites, Appl. Radiat. Isot. 71 (1) (2013) 62–67.
[25] A.M. El-Khatib, et al., Gamma attenuation coefficients of nano cadmium oxide/high density polyethylene composites, Sci. Rep. 9 (1) (2019) 1–11.
[26] L.B.T. La, et al., The interaction between encapsulated Gd_2O_3 particles and polymeric matrix: the mechanism of fracture and X-ray attenuation properties, Colloids Surf. A Physicochem. Eng. Asp. 535 (2017) 175–183.
[27] S. Jayakumar, T. Saravanan, J. Philip, Preparation, characterization and X-ray attenuation property of Gd_2O_3-based nanocomposites, Appl. Nanosci., 7 (8) (2017) 919–931.
[28] H.M.H. Zakaly, et al., Synthesis, optical, structural and physical properties of newly developed dolomite reinforced borate glasses for nuclear radiation shielding utilizations: an experimental and simulation study, Opt. Mater. 114 (2021), 110942 (Amst).
[29] F. Shahzad, et al., Electromagnetic interference shielding with 2D transition metal carbides (MXenes), Science 353 (6304) (2016) 1137–1140.
[30] L. Liang, et al., Promising Ti_3C_2Tx MXene/Ni chain hybrid with excellent electromagnetic wave absorption and shielding capacity, ACS Appl. Mater. Interfaces 11 (28) (2019) 25399–25409.
[31] M. Han, et al., Ti_3C_2 MXenes with modified surface for high-performance electromagnetic absorption and shielding in the X-band, ACS Appl. Mater. Interfaces 8 (32) (2016) 21011–21019.
[32] Q. Song, et al., Carbon nanotube–multilayered graphene edge plane core–shell hybrid foams for ultrahigh-performance electromagnetic-interference shielding, Adv. Mater. 29 (31) (2017), 1701583.
[33] J. Viegas, et al., Increased X-ray attenuation efficiency of graphene-based nanocomposite, Ind. Eng. Chem. Res. 56 (41) (2017) 11782–11790.
[34] M.J. Yaffe, et al., Composite materials for X-ray protection, Health Phys. 60 (5) (1991) 661–664.
[35] S. Nambiar, E.K. Osei, J.T.W. Yeow, Polymer nanocomposite-based shielding against diagnostic X-rays, J. Appl. Polym. Sci. 127 (6) (2013) 4939–4946.
[36] C.V. More, et al., Polymeric composite materials for radiation shielding: a review, Environ. Chem. Lett. 19 (3) (2021) 2057–2090.
[37] H. Mori, et al., Evaluation of the effectiveness of X-ray protective aprons in experimental and practical fields, Radiol. Phys. Technol. 7 (1) (2014) 158–166.
[38] M. Bat-Erdene, et al., Surface oxidized two-dimensional antimonene nanosheets for electrochemical ammonia synthesis under ambient conditions, J. Mater. Chem. A 8 (9) (2020) 4735–4739.
[39] C. Gibaja, et al., Few-layer antimonene by liquid-phase exfoliation, Angew. Chem. Int. Ed. 55 (46) (2016) 14345–14349.
[40] W. Lin, et al., A fast synthetic strategy for high-quality atomically thin antimonene with ultrahigh sonication power, Nano Res. 11 (11) (2018) 5968–5977.
[41] Q. Chen, B. Miao, Q. Ma, Sb_2O_3 functionalized plasmon, photoluminescence and Faraday rotation in glass, J. Non Cryst. Solids 545 (2020), 120251.
[42] K. Kaviyarasu, D. Sajan, P.A. Devarajan, A rapid and versatile method for solvothermal synthesis of Sb_2O_3 nanocrystals under mild conditions, Appl. Nanosci. 3 (6) (2013) 529–533.
[43] M.J. Nine, et al., Facile adhesion-tuning of superhydrophobic surfaces between "lotus" and "petal" effect and their influence on icing and deicing properties, ACS Appl. Mater. Interfaces 9 (9) (2017) 8393–8402.
[44] L.M. Johnson, et al., Elastomeric microparticles for acoustic mediated bioseparations, J. Nanobiotechnol. 11 (1) (2013) 22.
[45] G. Camino, S.M. Lomakin, M. Lazzari, Polydimethylsiloxane thermal degradation part 1. Kinetic aspects, Polymer 42 (6) (2001) 2395–2402 (Guildf).
[46] A. Akkaş, Determination of the tenth and half value layer thickness of concretes with different densities, Acta Phys. Pol. A 129 (4) (2016) 770–772.
[47] G.J. Scuderi, et al., Evaluation of non-lead-based protective radiological material in spinal surgery, Spine J. 6 (5) (2006) 577–582.
[48] N. Aral, F. Banu Nergis, C. Candan, An alternative X-ray shielding material based on coated textiles, Text. Res. J. 86 (8) (2016) 803–811.